

Annealing effects on interdiffusion in layered FA-rich perovskite solar cells

Cite as: AIP Advances **11**, 065327 (2021); <https://doi.org/10.1063/5.0046205>

Submitted: 03 February 2021 . Accepted: 09 June 2021 . Published Online: 23 June 2021

 D. O. Oyewole,  R. K. Koech, R. Ichwani,  R. Ahmed, J. Hinostrza Tamayo,  S. A. Adeniji, J. Cromwell, 
E. Colin Ulloa,  O. K. Oyewole,  B. Agyei-Tuffour,  L. V. Titova,  N. A. Burnham, and  W. O. Soboyejo



View Online



Export Citation



CrossMark

ARTICLES YOU MAY BE INTERESTED IN

[Pressure-assisted fabrication of perovskite light emitting devices](#)

AIP Advances **11**, 025112 (2021); <https://doi.org/10.1063/5.0035953>

[Impact of precursor concentration on the properties of perovskite solar cells obtained from the dehydrated lead acetate precursors](#)

Journal of Vacuum Science & Technology A **39**, 032801 (2021); <https://doi.org/10.1116/6.0000714>

[Pressure and thermal annealing effects on the photoconversion efficiency of polymer solar cells](#)

AIP Advances **11**, 045304 (2021); <https://doi.org/10.1063/5.0045694>



Call For Papers!

AIP Advances

SPECIAL TOPIC: Advances in
Low Dimensional and 2D Materials














Annealing effects on interdiffusion in layered FA-rich perovskite solar cells

Cite as: AIP Advances 11, 065327 (2021); doi: 10.1063/5.0046205

Submitted: 3 February 2021 • Accepted: 9 June 2021 •

Published Online: 23 June 2021



D. O. Oyewole,^{1,2}  R. K. Koeh,³  R. Ichwani,¹  R. Ahmed,¹  J. Hinostrza Tamayo,⁴  S. A. Adeniji,⁵ 
J. Cromwell,⁶  E. Colin Ulloa,⁴  O. K. Oyewole,^{1,6}  B. Agyei-Tuffour,⁷  L. V. Titova,⁴  N. A. Burnham,⁴ 
and W. O. Soboyejo^{1,6,a)} 

AFFILIATIONS

¹ Materials Science and Engineering Program, Department of Mechanical Engineering, Worcester Polytechnic Institute, 100 Institute Road, Worcester, Massachusetts 01609, USA

² Physics Advanced Research Center, Sheda Science and Technology, Km 10 Abuja-Lokoja Road, P.M.B 186, Garki-Abuja, Federal Capital Territory, Nigeria

³ Department of Materials Science and Engineering, African University of Science and Technology, Km 10 Airport Road, Galadimawa, P.M.B. 681, Garki-Abuja, Federal Capital Territory, Nigeria

⁴ Department of Physics, Worcester Polytechnic Institute, 100 Institute Road, Worcester, Massachusetts 01609, USA

⁵ Department of Theoretical and Applied Physics, African University of Science and Technology, Km 10, Airport Road, Galadimawa, P.M.B. 681, Garki-Abuja, Federal Capital Territory, Nigeria

⁶ Department of Mechanical Engineering, Worcester Polytechnic Institute, 100 Institute Road, Worcester, Massachusetts 01609, USA

⁷ Department of Materials Science and Engineering, School of Engineering Sciences, University of Ghana, Legon-Accra, Ghana

^{a)} **Current address:** Program in Materials Science and Engineering, Worcester Polytechnic Institute, 100 Institute Road, Worcester, Massachusetts 01609, USA. **Author to whom correspondence should be addressed:** wsoboyejo@wpi.edu.

Tel.: +1 508 831 5448

ABSTRACT

Annealing is one of the processing methods that are used for the fabrication of defect-free, photoactive perovskite films with compact grains in highly efficient and stable perovskite solar cells (PSCs). Thus, the annealing temperature is a key parameter for the control of the interdiffusion (of constituent elements) in photoactive films. In this paper, we present the results of a systematic study of the effects of annealing on the interdiffusion of constituent elements in efficient formamidinium-based PSCs. We also explore the effects of annealing-induced interdiffusion on layer microstructures, local strains, and the optoelectronic properties of perovskite films. We observe a dramatic upward diffusion of tin (Sn) and titanium (Ti) from fluorine-doped tin oxide and titanium dioxide (TiO₂) to the perovskite films. We also observe a downward diffusion of lead (Pb) and iodine (I) from the perovskite films to the mesoporous layer of the electron transporting layer (ETL), after annealing at temperatures between 100 and 150 °C. The diffused I substitutes for Ti in the ETL, which improves the optoelectronic properties of the films, for annealing temperatures between 100 and 130 °C. The annealing-induced interdiffusion that occurs at higher temperatures (between 140 and 150 °C) results in higher levels of interdiffusion, along with increased local strains that lead to the nucleation of pores and cracks. Finally, the implications of the results are discussed for the design of PSCs with improved photoconversion efficiencies and stability.

© 2021 Author(s). All article content, except where otherwise noted, is licensed under a Creative Commons Attribution (CC BY) license (<http://creativecommons.org/licenses/by/4.0/>). <https://doi.org/10.1063/5.0046205>

I. INTRODUCTION

Over the past decade, lead-based organic–inorganic hybrid perovskites have received significant attention as absorber materials in perovskite solar cells (PSCs).^{1–11} Significant improvements have also been made in the performance and stability of perovskite solar cells in the same period. These have been achieved via process engineering,^{12,13} compositional control,^{14–18} the use of different layered architectures,^{4,19,20} and the application of different deposition techniques to achieve power conversion efficiencies (PCEs) in excess of 25%.²¹

Such high PCE values have been attributed largely to the properties of the photoactive perovskite material, which includes: long-range charge carrier diffusion lengths,^{22,23} highly tunable bandgaps,^{16,24} low exciton binding energies,^{8,25} and high absorption over a wide range of wavelengths.^{18,19} Hence, perovskite solar cells are considered as promising thin film photovoltaic systems that are more cost-effective^{26,27} than their silicon-based counterparts.

The materials for perovskite solar cells (PSCs) have been improved from the initial single cation methylammonium lead iodide (MAPbI₃)¹ to formamidinium lead iodide (FAPbI₃),³ and a combination of inorganic cesium and organic materials.^{14,28} The resulting formamidinium-based perovskite solar cells have been shown to have a broader solar spectrum absorption, thereby giving rise to improved photoconversion efficiencies.^{11,14,17,29,30} In addition, by varying the combination of cations, we can now narrow the bandgaps of the perovskite layers and thus improve their thermal stability.¹⁹

Furthermore, solution processing techniques have made the fabrication of organic–inorganic hybrid perovskite solar cells easier and more attractive.^{4,19,31,32} Thus, simpler processing techniques, which involve a single annealing step, have been developed to convert spin-coated perovskite precursor solutions into crystalline perovskite films. The morphologies and crystallinity of the resulting perovskite films have also been shown to be dependent on the annealing temperature, which have a direct impact on their overall power conversion efficiencies.^{26,30,33} Hence, annealing methods have become important in the engineering of perovskite solar cells with improved PCEs.^{34–37}

Thermal annealing processes are very critical steps that have been used to tune the morphologies of perovskite films.²⁶ These include multistep slow annealing methods to achieve very reproducible solar cells,³⁸ a low temperature gradual annealing method for the controlled crystallization of perovskites (leading to homogeneous film formation),³⁹ and complete conversion into perovskite films (from precursor solutions) via thermal annealing, without the need for additives to stabilize the perovskite lattice.³⁶

Thermal annealing of perovskite films has also been shown to be accompanied by the formation of charged vacancies at the surfaces and the grain boundaries of perovskite films,⁴⁰ while passivation techniques^{28,41–43} have been used for reducing the defect content, which also improves the PCEs of perovskite solar cells.

Furthermore, interdiffusion has been explored as a method^{28,41,44–48} for the production of phase stable, large grained, and pin-hole free⁴⁹ perovskite films. The crystallization and growth of continuous, compact, perovskite films have been controlled by adjusting reactant concentrations⁴⁸ and also by increasing annealing durations.^{41,45,50} Annealed PSCs have also been optimized by varying the concentrations of halides in the precursor solutions,^{40,41,44,45}

while the diffusion of dopants into the hole transporting layers (HTLs) of organometallic halide perovskite solar cells has been used to significantly improve charge transport and photoconversion efficiency.^{51,52} Furthermore, oxygen vacancies in the electron transporting layer (ETL) have been shown to create donor states below the conduction band, resulting in an improved band alignment with the perovskite layer, which can improve charge extraction.^{53,54}

In this study, we explore the effects of thermal annealing on the interdiffusion of elements in formamidinium-rich lead mixed halide perovskite solar cells. The upward and downward diffusion of elements is elucidated using Energy Dispersive X-ray spectroscopy (EDX), Scanning Electron Microscopy (SEM), and X-Ray Diffraction (XRD) techniques. The resulting microstructures are characterized to develop an in-depth understanding of the effects of annealing on the interdiffusion of constituent elements, annealing-induced strains, and the optoelectronic properties of perovskite solar cells. The implications of the results are discussed for the fabrication of efficient perovskite solar cells.

II. MATERIALS AND METHODS

A. Materials

Fluorine-doped tin oxide (FTO)-coated glass ($\sim 7 \Omega \text{ sq}^{-1}$), lead iodide (PbI₂) (99.999%), diisopropoxide bis(acetylacetonate), formamidinium iodide (FAI) (98%), methylammonium chloride (MACl), methylammonium bromide (MABr) (98%), dimethylformamide (DMF), dimethylsulfoxide (DMSO), titania paste, 1-butanol, ethanol, iso-propyl alcohol (IPA), 4-tert-butylpyridine (tBP), acetonitrile, lithium bis(trifluoromethylsulfonyl) imide (Li-TFSI), 2,2',7,7'-tetrakis(N,N-di-*p*-methoxyphenylamine)-9,9'-spirobifluorene (Spiro-OMeTAD), and anhydrous chlorobenzene were all purchased from Sigma-Aldrich (Natick, MA, USA). All the materials were used in their as-received conditions.

B. Materials processing and PSCs fabrication

The FTO-coated glass was patterned by etching using zinc powder and 2M hydrochloric acid and sonicated successively (each for 15 min) in deionized water, acetone (Sigma-Aldrich), and IPA (Sigma-Aldrich). The cleaned substrates were then blow-dried in nitrogen gas, prior to UV–ozone cleaning (Novascan, Main Street Ames, IA, USA) for 15 min to remove organic residuals.

An electron transporting layer (ETL) (that comprises compact and mesoporous layers of titanium oxide) was deposited onto FTO-coated glass, following the previous protocol.⁵⁵ The compact titanium oxide (*c*-TiO₂) was spin-coated onto the cleaned FTO-coated glass from a 0.15M solution of titanium diisopropoxide bis(acetylacetonate) in 1-butanol at 2000 rpm for 30 s. This was annealed at 150 °C for 5 min before spin coating the 0.3 M solution of titanium diisopropoxide bis(acetylacetonate) in 1-butanol at 2000 rpm for 30 s. The deposited *c*-TiO₂ was then sintered in a furnace (Lindberg Blue M, Thermo Fisher Scientific) at 500 °C for 30 min. The sample was then allowed to cool down to room temperature ($\sim 22 \text{ }^\circ\text{C}$). Subsequently, a mesoporous titanium oxide (*m*-TiO₂) layer was spin coated from a mixture of titania paste and ethanol in ratio 1:5 (w:w) at 5000 rpm for 30 s before sintering at 500 °C for 1 h in a furnace (Lindberg Blue M, Thermo Fisher Scientific).

Lead iodide solution was prepared by mixing 0.5993 g of PbI_2 and DMF:DMSO (9.5:0.5; v:v). The solution was stirred using a magnetic stirrer at 500 rpm for 2 h at 60 °C heating temperature. The mixture was filtered through a 0.45 μm mesh filter before spin-coating onto the mesoporous TiO_2 at 1500 rpm for 30 s. The film was then annealed at 70 °C for 1 min and allowed to cool down to room temperature.

Thereafter, a formamidinium-rich organic component of the perovskite film was prepared. This consists of 60 mg of FAI, 6 mg of MABr, and 6 mg of MACl in 1 ml of IPA. The mixture was sonicated for 30 min to allow the salts to fully dissolve. The solution was then spin-coated onto the PbI_2 layer at 1300 rpm for 30 s. The films were annealed at various temperatures (100, 120, 130, 140, and 150 °C). We also took the *in situ* videos of the films during annealing using a high resolution Proscope digital microscope (Proscope HR, Bodelin Technologies, OR, USA). The annealing-induced strains were then estimated using a digital image correlation technique. Some of the annealed perovskite films were set aside for characterization, while a hole transporting layer (HTL) was spin coated onto the films for PSC devices.

For fabrication of PSC devices, the HTL was prepared by first dissolving 260 mg of Li-TFSI in 1 ml of acetonitrile. Then, 72 mg of Spiro-OMeTAD was dissolved in 1 ml of chlorobenzene before adding 30 and 35 μl of tBP and Li-TFSI solutions, respectively. The mixture was then sonicated for 5 min before spin coating onto the perovskite films at 4000 rpm for 30 s. Finally, a 90 nm thick gold layer was thermally evaporated onto the films using an Edward E306A evaporation system (Edward E306A, Easton PA, USA). The evaporation was carried out at a vacuum pressure of $\sim 1 \times 10^{-6}$ Torr and a deposition rate of 0.2 nm s^{-1} . A shadow mask was used to define a device area of 0.1 cm^2 .

C. Characterization

The optical absorbance of the perovskite films (for the various annealing temperatures) was measured using an Avantes UV-Vis spectrophotometer (Avantes, BV, USA). The resulting microstructures of the top surfaces and cross sections of the films were observed using a field emission gun scanning electron microscope (SEM) (JSM 7000F, JOEL Ltd., Tokyo, Japan), while the concentration gradients of the elements were obtained along with energy dispersive x-ray spectra using an energy dispersive x-ray spectrometer (Oxford Instrument, UK). The XRD patterns of the perovskite films were obtained using an x-ray diffractometer (XRD) (Malvern PANalytical, Westborough, MA, USA) under a $\text{Cu K}\alpha$ radiation source with Beta Nickel filter at 40 KV and 40 mA.

The current density–voltage curves were measured for all the PSC devices that were prepared at different annealing temperatures. These were obtained using a Keithley source meter unit 2400 system (Keithley, Tektronix, Newark, NJ, USA) that was connected to an Oriol solar simulator (Oriol, Newport Corporation, Irvine, CA, USA). The devices were exposed to AM1.5G illumination of 90 mW cm^{-2} during the current density–voltage measurements. The illumination from the solar simulator was calibrated using a 918D high performance calibrated photodiode sensor (918D Photon detector, Newport).

III. RESULTS AND DISCUSSION

A. Interdiffusion of constituent elements in perovskite solar cells

During PSC fabrication, compact and mesoporous TiO_2 layers are deposited onto FTO glass substrates and sintered at 500 °C. This resulted in the leaching and diffusion of Sn from the FTO substrate into the TiO_2 matrix during the sintering process. After the deposition of the perovskite film, the resulting samples were annealed at temperatures between 100 and 150 °C. The elements in the perovskite layer [specifically lead (Pb) and iodine (I)] diffused into the mesoporous TiO_2 layer, thus changing the material properties of the electron transporting layer.

To investigate and quantify the interdiffusion of constituent elements, due to the thermal annealing of the perovskite film in different layers of the PSCs, the diffusion of the constituent elements was tracked using EDX during the SEM imaging of the layered structures of the PSCs. Figure 1(a) presents a representative cross-sectional SEM image that shows the EDX mapped area within the *m*- TiO_2 layer. More cross-sectional SEM images of the multilayered structures are presented in Figs. S1(a)–S1(e), [supplementary material](#), for different annealing temperatures between 100 and 150 °C. Representative EDX spectra of the mesoporous TiO_2 layer and the perovskite layers are presented in Figs. S2(a) and S2(b).

The interdiffusion of elements is observed across the various layers that make up the PSCs during perovskite thermal annealing. The *m*- TiO_2 layer shows significant changes in the elemental composition [Figs. 1(b)–1(e)] at different annealing temperatures. It is evident that the elements from the perovskite film diffused downward toward the ETL, while elements from the FTO layer diffused upward into the ETL. Measured Pb levels (from the perovskite film into the ETL) increased from ~ 10 to 28.1 wt. %, while the level of I increased from ~ 11 to ~ 39 wt. %, as the annealing temperature increased from 100 to 130 °C [Figs. 1(b) and 1(c)]. Figure 1(c) shows the increasing iodine content, as the annealing temperature increased up to 130 °C. It then drops with a further increase in temperature. This peak level suggests a maximum doping concentration of iodine within the ETL, for improved charge extraction at 130 °C.⁵⁶ This enhanced charge extraction of PSCs can, therefore, lead to improved performance characteristics.

Moreover, the downward diffusion of Pb and I into the ETL reduces the levels of O and Sn, for annealing temperatures between 100 and 130 °C [Figs. 1(b) and 1(c)]. The oxygen vacancy in *m*- TiO_2 increased [Fig. 1(d)] with increasing annealing temperature, which is very important for improved optical properties.⁵⁷ Hence, low oxygen levels in the *m*- TiO_2 lead to increased electron doping density.⁵⁷ The doping of the ETL, with elements from perovskite films, can also lead to improved charge extraction in the solar cells.⁵⁸

The titanium (Ti) contents are presented in Fig. 1(e), along with a summary of percentage composition–annealing temperature plots [Fig. 1(f)] of the major elements in the *m*- TiO_2 layer. It is important to note here that the percentage compositions of Ti and I mirror each other, as the composition of Ti decreases with increasing temperature from 100 to 130 °C. The Ti content then increases for structures annealed at temperatures between 140 and 150 °C.

Interestingly, the EDX map of the top surface of the photoactive perovskite layer [Fig. 2(a)] shows that Ti and Sn diffuse upward from the FTO and TiO_2 layers. The Ti and Sn levels in the perovskite

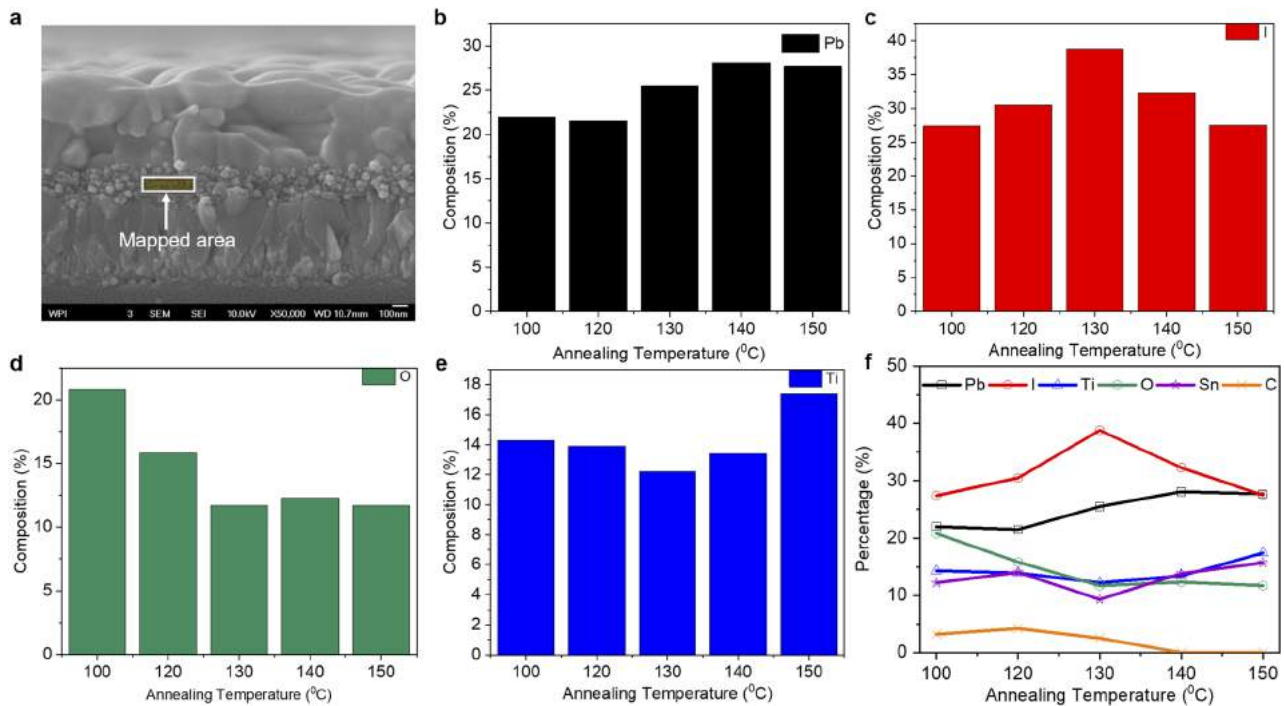


FIG. 1. (a) A representative cross-sectional SEM image of PSC structures, showing an EDX mapped region within the mesoporous TiO₂ layer, (b)–(e) percentage compositions of Pb, I, O, and Ti, and (f) summary of percentage composition–annealing temperature plots for all major elements.

layer also increase with increasing temperature [Figs. 2(b) and 2(c)], which can change the texture and crystal lattice of the perovskite films.

The diffusion of elements in perovskite films can be elucidated using elemental concentration gradient and profile.⁵⁹ We further provide insights into the concentration gradient and profile of the perovskite film using the image of the EDX map of the cross section [Fig. 3(a)] of the layered structure. Figures 3(b)–3(e) present the concentration gradients of Sn, Ti, Pb, and I that are aligned with the layers of FTO, TiO₂, and perovskite films in the SEM image [Fig. 3(a)] along with their concentration profiles [Fig. 3(f)]. The concentration profile was obtained by extracting the brightest pixels of the EDX images using a MATLAB code. The concentration

profiles of Sn, Ti, and I are presented in Figs. 3(g)–3(i) for different annealing temperatures. We see an overall upward diffusion of Sn and Ti from FTO and TiO₂ to the perovskite layer, respectively. The concentration profile of I [Fig. 3(i)] also shows a downward diffusion of iodine in perovskite to the TiO₂ layer.

B. Effects of annealing on microstructures of perovskite films

The SEM images [Figs. 4(a)–4(e)] clearly show that the microstructural morphologies of the perovskite films are highly dependent on the annealing temperature. Perovskite films annealed at 100 °C [Fig. 4(a)] had a large number of small grains. Grain growth was also observed when the annealing temperature was

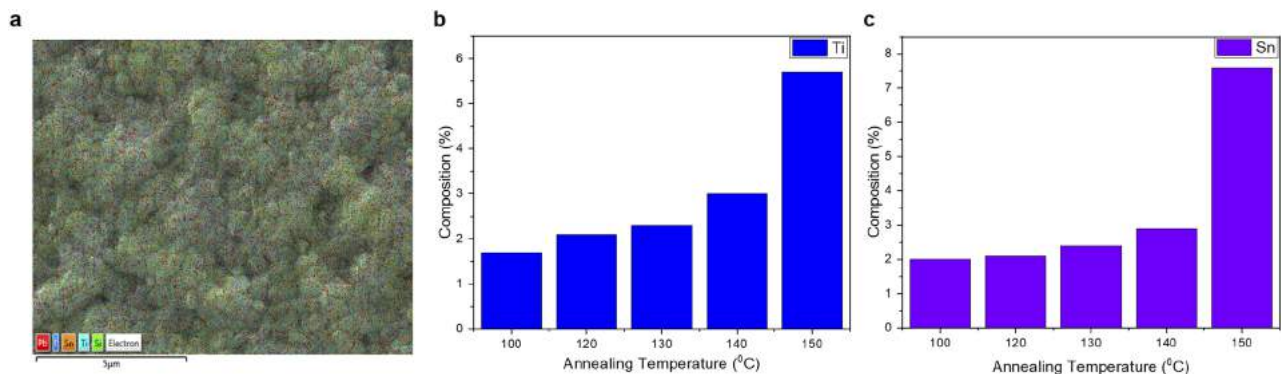


FIG. 2. (a) Representative SEM/EDX map of the top surface of perovskite films and (b) and (c) percentage composition of Ti and Sn at the top of the perovskite film.

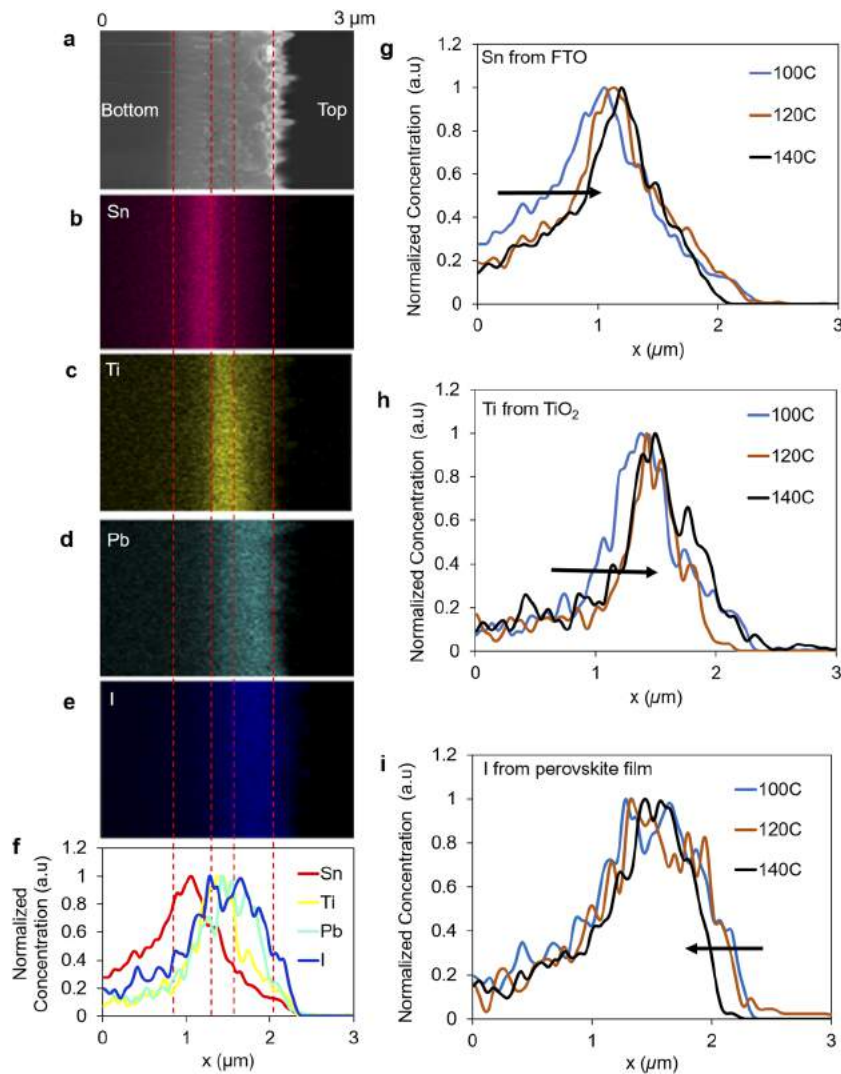


FIG. 3. Concentration gradients and profiles of elemental diffusion within PSC structures: (a) cross-sectional SEM image of the PSC structure annealed at 120 °C; (b)–(e) images of EDX maps that show concentration gradients of Sn, Ti, Pb, and I; (f) concentration profile of Sn in FTO, Ti in TiO₂, and Pb and I in perovskite films, and (g)–(i) concentration profiles of Sn from FTO (g), Ti from TiO₂ (h), and I from perovskite (i) at different annealing temperatures.

increased up to 130 °C. This resulted in a densely interconnected network of grains [Figs. 4(b) and 4(c)]. Annealing at 140 °C revealed a number of large, irregularly shaped, plate-like grains [Fig. 4(d)]. The resulting films were rougher, with larger grain sizes than those observed in the perovskite films annealed at lower temperatures.

In the case of perovskite films annealed at 150 °C, we see a formation of large grains with voids between them, thus revealing the *m*-TiO₂ layer underneath [Fig. 4(d)]. It is also important to note that the seemingly exposed areas of *m*-TiO₂ are still covered with a very thin layer of perovskite film, which allows for the structure to be transparent to electrons during electron microscopy. The formation of voids can be associated with rapid growth of grains from a few nucleation sites. The mean grain area of the perovskite film was estimated from SEM images using the ImageJ software. The distribution plot of the perovskite grain areas is presented in Fig. 4(f) for the different annealing temperatures. The mean grain area of the perovskite film increases from 0.103 to 0.471 μm², as the annealing temperature increased from 100 to 150 °C. More grain area distribution plots are presented in Figs. S3(a)–S3(e), [supplementary](#)

[material](#). We see an increase in the grain area with increasing annealing temperature from 100 to 150 °C.

C. Annealing effects on optical properties and structure of PSCs

The optical absorbance of the photoactive perovskite film was measured using a UV-VIS spectrometer. The UV-VIS absorption spectra of the films are presented in Fig. 5(a). We see increased absorption with increasing annealing temperature from 100 to 130 °C [Fig. 5(a), inset I]. A further increase in the annealing temperature leads to reduced absorption of light. No clear absorption peaks were observed for films that were annealed at 150 °C [Fig. 5(a), inset II]. These changes in light absorption of the perovskite films are attributed to phase changes in perovskite, morphology changes in the films, as well as changes in grain sizes with increased annealing temperature. A redshift is also observed with increasing temperature up to 140 °C.

Figure 5(b) presents the steady state photoluminescence (PL) spectra obtained for the perovskite absorber films annealed between

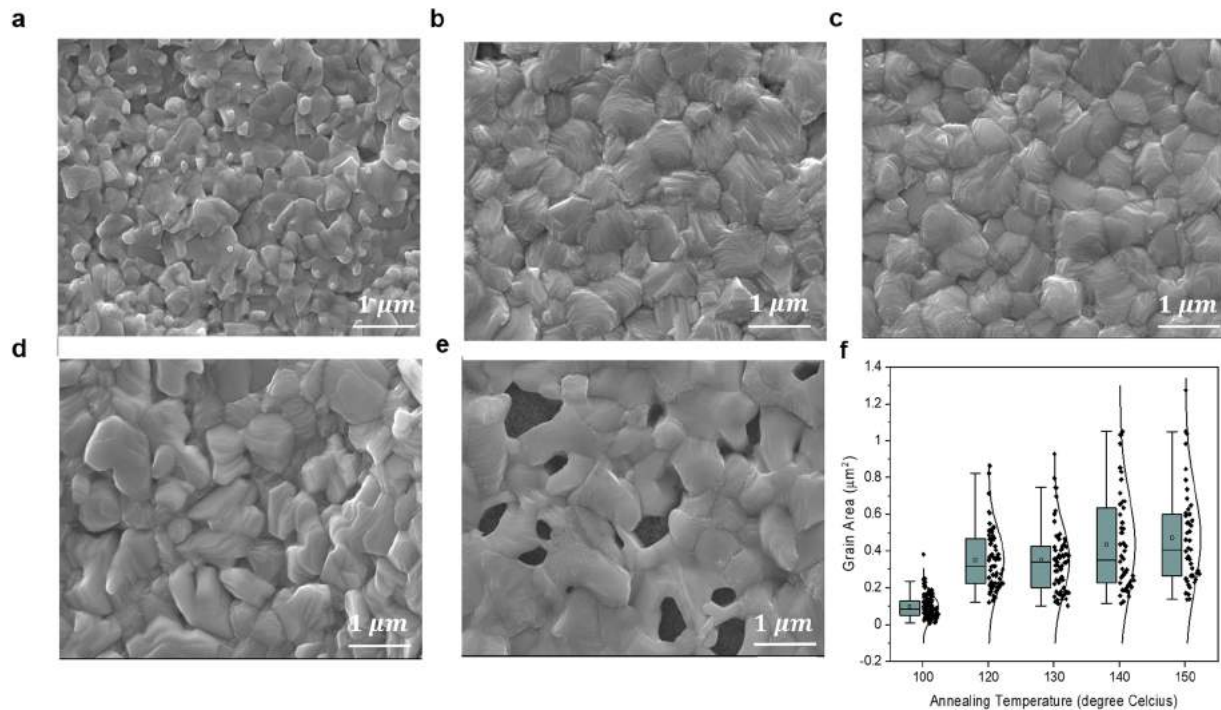


FIG. 4. (a)–(e) SEM images of perovskite films annealed at 100 °C (a), 120 °C (b), 130 °C (c), 140 °C (d), and 150 °C (e) and (f) box-and-whisker plot showing grain area distribution at different temperatures.

100 and 140 °C. No peak was observed for the film annealed at 150 °C. This can be attributed to decomposition of the absorber film at such a high temperature. It can also be associated with sporadic formation of large pinholes in the absorber [Fig. 4(e)]. The peaks of the PL intensity reduced with increasing annealing temperature, for the perovskite films annealed between 100 and 130 °C [Fig. 5(b), inset I]. This reduction in the PL peaks is attributed to the changes in the crystallinity of the perovskite film that occur with increasing annealing temperature. It is also associated with the improved charge extraction characteristics that are associated with thermal annealing at temperatures up to 130 °C.

However, for the film annealed at 140 °C, the PL intensity significantly increased [Fig. 5(b), inset II]. This increase is evident in defect formation and pin holes in the perovskite film when annealed beyond 130 °C. This can lead to poor charge extraction due to recombination at defect sites. The improved crystallinity and change in the grain size of the perovskite films, due to thermal annealing, can enhance the oscillating strength of optical transitions,⁶⁰ which can lead to changes in internal reflections of emitted light,^{61,62} and hence change the luminescence property of the films.

Figure 5(c) presents the normalized PL spectra. This shows a redshift of the PL spectra peaks with increasing annealing temperature from 100 to 150 °C, which is consistent with the absorption spectra. The peak shifts from 797 to 811 nm wavelengths, with corresponding optical bandgaps reducing from 1.56 to 1.53 eV.

To further study charge carrier dynamics, we measured the time resolved photoluminescence (TRPL) on the perovskite films annealed at different temperatures. The TRPL gives access to recombination pathways while also providing quantitative information on

recombination rates. Figure 5(d) presents the TRPL of the films for different annealing temperatures. The lifetime of charge carriers in the perovskite films is increased when annealed between 100 and 130 °C. Recombination rates of charge carriers were estimated by fitting TRPL data into a bimolecular recombination function,

$$n(t) = \frac{n(0)}{(1 + at)^2}, \quad (1)$$

where a is the bimolecular recombination rate, $n(0)$ is the peak amplitude of the TRPL, t is time, and $n(t)$ is the instantaneous TRPL. Both the bimolecular recombination rates and peak amplitude reduce with increasing annealing temperature between 100 and 130 °C (Table I).

The reduction in the bimolecular rate is an indication of lower charge carrier recombination due to large compact grain formation and less trap states in the perovskite films annealed between 100 and 130 °C temperatures. Perovskite films formed at higher temperatures have larger grain sizes, which can drastically reduce the overall bulk defect density and hence reduce recombination. However, the increased bimolecular rate observed for 140 °C (Table I) can be attributed to more bulk and surface recombination of free charge carriers^{63,64} due to increased defects, which is evident in the SEM images [Figs. 4(d) and 4(e)].

In order to gain insights into the structure and crystallinity of the perovskite absorber films that were annealed at different temperatures, we obtained x-ray diffraction patterns of the films using x-ray diffractometry (XRD). Figures 5(e) and 5(f) present strong and sharp diffraction peaks for all the samples, showing good crystallinity for

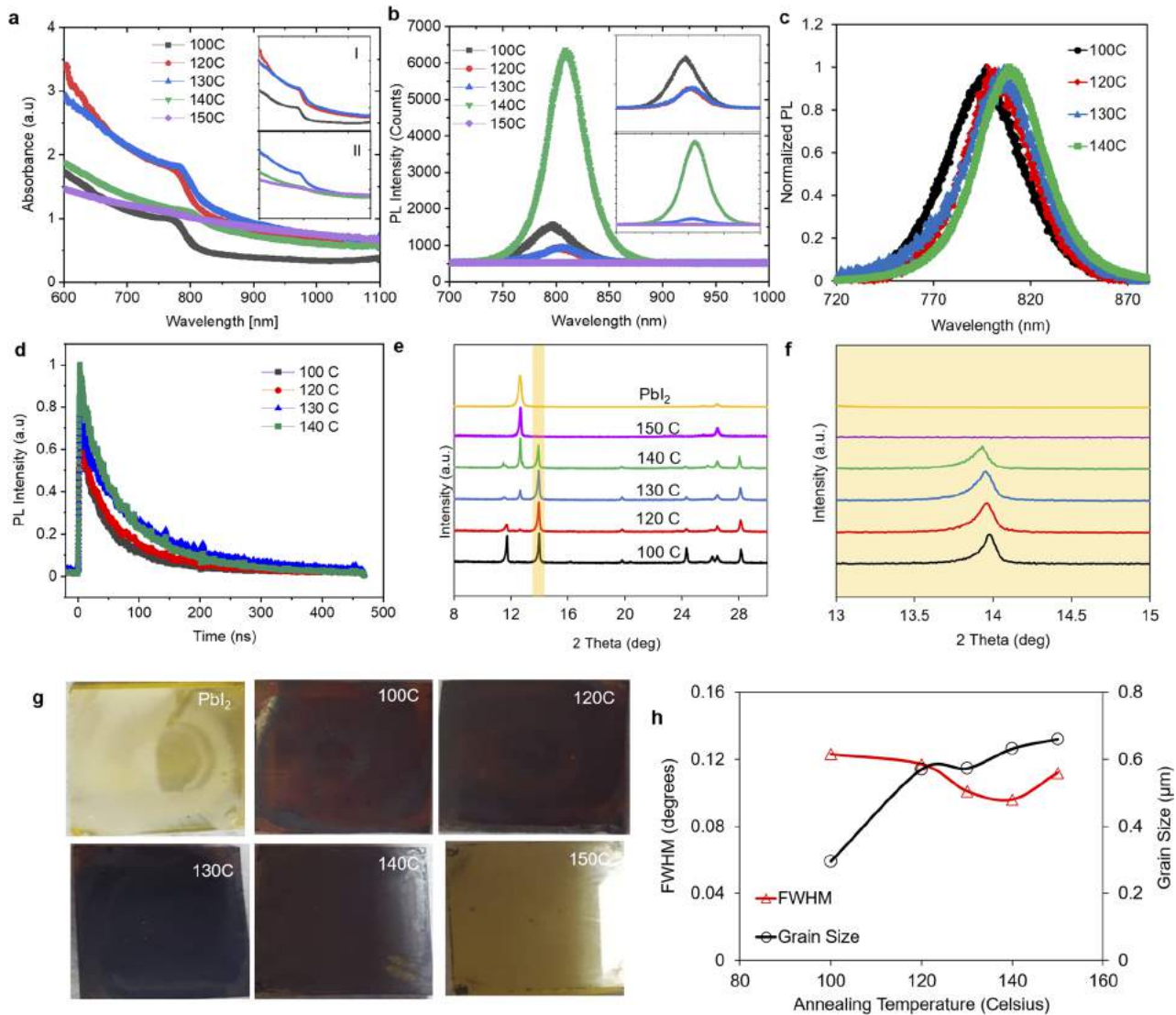


FIG. 5. (a) Optical absorption spectra of the films annealed at different temperatures between 100 and 150 °C, with an inset that compares the absorbance of films annealed from 100 to 130 °C (inset I) and films annealed from 130 to 150 °C (inset II); (b) PL spectra of perovskite multilayer films annealed at different temperatures between 100 and 150 °C, with insets I and II that compare the PL spectra of films annealed from 100 to 130 °C and from 130 to 150 °C, respectively; (c) normalized PL spectra of films annealed at different temperatures; (d) time resolved PL decay of films annealed at different temperatures; (e) XRD patterns of the PbI_2 film and perovskite films annealed at different temperatures; (f) magnified XRD patterns of the α -phase of the perovskite films annealed at different temperatures; (g) images of the prepared PbI_2 film and perovskite films annealed at different temperatures; and (h) plots of FWHM and grain size vs annealing temperatures. Each of the data for the grain size represents the average value of the measured grain sizes of films.

TABLE I. Bimolecular recombination rates and TRPL peak amplitudes at different annealing temperatures.

Annealing temperature (°C)	a (ns) ⁻¹	$n(0)$ (counts)
100	0.018	263.6
120	0.012	246.0
130	0.008	246.5
140	0.011	324.9

all the absorber films. The diffraction peaks obtained for all films at 2θ values of 26.9° , 34.06° , 37.94° , and 51.7° correspond to the peaks from FTO glass having lattice planes of (110), (101), (200), and (211), respectively.⁶⁵ The 2θ values of 14° , 20.1° , 24.41° , 28.2° , 31.67° , and 43.4° correspond, respectively, to (110), (012), (111), (220), (310), and (314) lattice planes for the perovskite tetragonal phase.^{66,67}

When the double cation (FA and MA) mixed halide organic components are mixed with PbI_2 , a dark chocolate cubic perovskite phase is formed upon thermal annealing. The chocolate color of the

cubic perovskite phase becomes darker as the annealing temperature is increased from 100 to 130 °C. A yellowish hexagonal perovskite phase is formed at higher temperatures between 140 and 150 °C [Fig. 5(g)]. At 150 °C, a different crystal structure is present along with the cubic PbI_2 phase. This is evident in Fig. 5(e), in which the annealed perovskite films show decreasing intensity of perovskite peaks, while the PbI_2 peak (at $2\theta = 12.7^\circ$) increases with increasing annealing temperature. The decrease in the intensity of perovskite peaks suggests a possible change in grain sizes and a preferred crystal orientation.⁶⁸

The peaks observed at a 2θ value of $\sim 12^\circ$ (010) show the formation of the δ -perovskite phase,⁶⁹ as seen in some of the annealed films. In addition, the presence of a sharp intense diffraction peak obtained from the perovskite films at a 2θ value of 14° indicates the presence of a pure α -perovskite phase.^{16,69} This peak shows a shift to lower diffraction angles with an increase in the annealing temperature [Fig. 5(f)]. This shift is an indication of the perovskite lattice expansion due to increased annealing temperature. The characteristic diffraction peaks of both the α phase and the δ phase of the perovskite are not observable in the diffraction patterns obtained for the films annealed at temperatures above 140 °C. This suggests a complete conversion of both the α and δ phases, since all of the diffraction peaks (of both perovskite phases) disappeared after annealing at 150 °C. The peaks of the perovskite films annealed at 150 °C correspond to those of the cubic PbI_2 phase [Fig. 5(e)], indicating complete decomposition of the perovskite film to PbI_2 at higher temperatures. This is also evident in the conversion of the dark chocolate color of the perovskite film to a yellow color, after annealing at 150 °C [Fig. 5(g)]. The estimated Full Width at Half Maximum (FWHM) of the films [Fig. 5(h)] decreases with increasing temperature between 100 and 140 °C. This is evident in the increased grain sizes of the films [Fig. 5(h)]. We see a slight increase in the FWHM of the films at 150 °C due to the presence of large voids.

D. Evolution of annealing-induced strains during interdiffusion process

To gain insights into the strains induced during the interdiffusion processes that occur during the annealing of the perovskite

films, we took high resolution videos of *in situ* microscopic images of the films during the annealing. These videos were processed to extract the local strains in the films using a digital imaging correlation technique.^{70,71} We see increased transverse, longitudinal, and shear strains in the films with increasing annealing temperature [Figs. 6(a)–6(c)] in both tension and compression. The increased strains are associated with increasing lattice expansion [Fig. 5(f)] and grain sizes [Figs. 4(a)–4(e)], as the annealing temperature is increased from 100 to 150 °C. At 150 °C, the transverse [Fig. 6(a)], longitudinal [Fig. 6(b)], and shear [Fig. 6(c)] strains in the film increased drastically within a short period of time. This rapid increase in strain results in cracking or pore formation [Fig. 4(e)].

The processed images of the films show how the strains increase with time for transverse [Fig. 7(a)], longitudinal [Fig. 7(b)], and shear [Fig. 7(c)] strains. It is important to note that the regions of high tension correspond to yellow and red colors, while the blue color corresponds to compression. There are local strain effects at low temperatures, while the strains are concentrated at higher temperatures. Furthermore, as the annealing temperature increases from 100 to 150 °C, the strains in the evolving grains are associated with thermal expansion mismatch of the different materials that are interdiffused during the annealing process.

E. Electrical properties of the PSCs

To elucidate the implications of the annealing-induced interdiffusion on the electrical properties of PSCs, we characterized the current–voltage characteristics of PSC devices that were fabricated at different annealing temperatures. Figure 8(a) shows the current density–voltage (J - V) curves of the PSCs prepared at annealing temperatures that range from 100 to 150 °C. The inset of Fig. 8(a) presents the device structure, indicating the device active area. There is an increase in the short circuit current density with increasing annealing temperatures between 100 and 130 °C [Fig. 8(b)]. The power conversion efficiencies (PCEs) and the open circuit voltage (V_{oc}) of the devices prepared at different annealing temperatures are also presented in Figs. 8(c) and 8(d). The histograms and distribution curves of PCEs for devices annealed at different

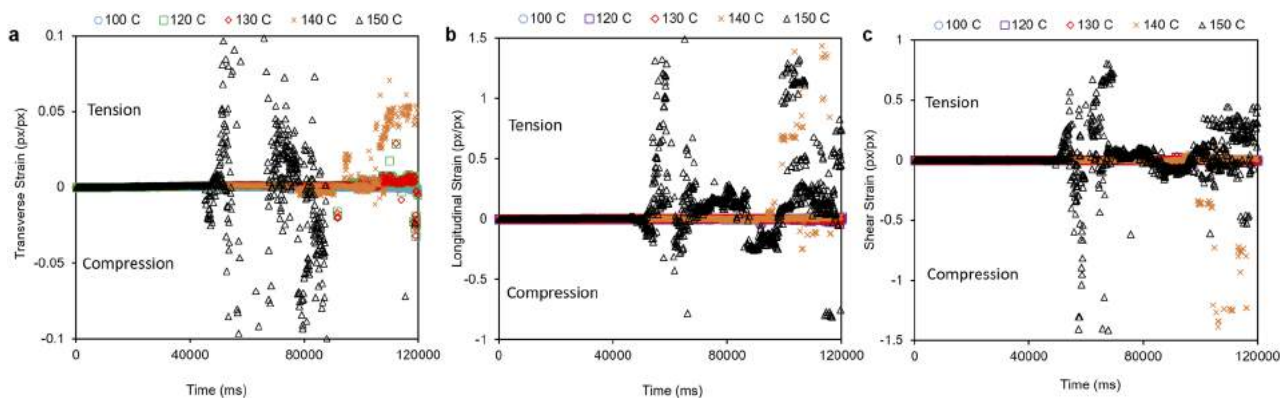


FIG. 6. Strains of perovskite films during the annealing-induced interdiffusion process for both tension and compression: (a) transverse, (b) longitudinal, and (c) shear strains.

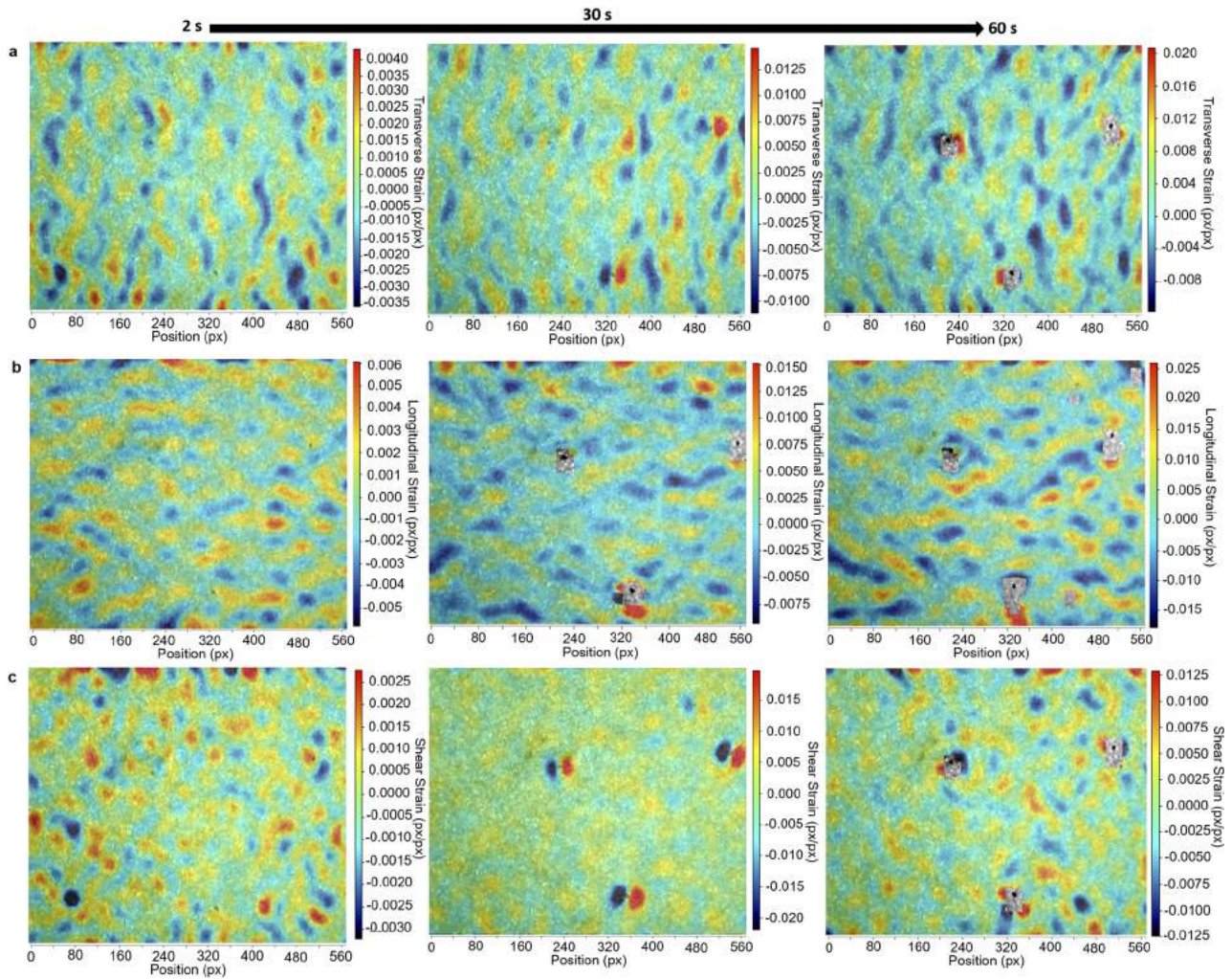


FIG. 7. Representative DIC images of the strain distributions for 130 °C annealed perovskite films: (a) transverse strain, (b) longitudinal strain, and (c) shear strain. The images show strain distributions at different times: 2, 30, and 60 s.

temperatures are presented in Fig. S4, [supplementary material](#). The devices show increased performance characteristics from 100 to 130 °C. The best performing cells are samples that were annealed at 130 °C, giving a PCE of 19.4% that corresponds to a J_{sc} of 24.1 (mA cm^{-2}), V_{oc} of 1.08 V, and FF of 0.69. However, annealing at higher temperatures (140 and 150 °C) results in lower device performance characteristics. Figures S4(a)–S4(e) show the distribution of PCEs obtained for devices annealed at temperatures that range from 100 to 150 °C. The device parameters are summarized in [Table II](#). A clear correlation is observed between annealing temperatures and the device performance characteristic parameters.

The improved PCEs are associated with a significant increase in the grain sizes of the perovskite films, as well as the upward and downward diffusion of materials within ETL and perovskite, respectively. The increased PCEs of the devices annealed between 100 and

130 °C are also associated with the doping of iodine within the ETL. This enhances charge extraction, as shown in the PL spectra [[Fig. 5\(b\)](#)] of the perovskite films. Moreover, the increased vacancy of oxygen in the $m\text{-TiO}_2$,²³ due to the downward diffusion of lead and iodine from the perovskite layer [[Figs. 1\(b\)](#) and [1\(c\)](#)], is evident in the absorption. This explains the increased PCEs of the devices that were annealed at 100–130 °C. However, the decrease in the PCEs of the devices that were annealed at 140 °C and 150 °C is attributed to the effects of cracks and pores [[Figs. 4\(d\)](#) and [4\(e\)](#)] that were induced by local strain concentrations [[Figs. 7\(a\)–7\(c\)](#)] and interdiffusion processes. It is also important to note that a decrease in the recombination of charge carriers [[Table I](#)] is also evident in the enhanced performance characteristics of the PSC devices that were annealed at temperatures up to 130 °C. However, the defects that are formed at higher temperatures act as carrier trap sites, which decrease the device PCEs.

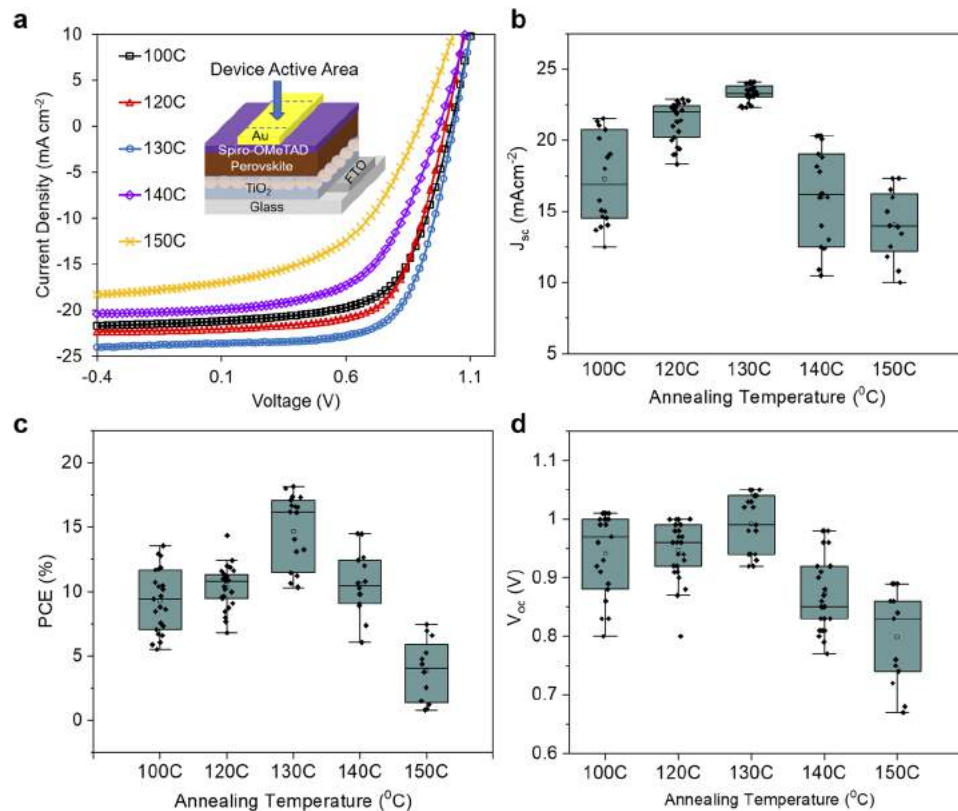


FIG. 8. (a) Current density–voltage curves of perovskite solar cells that were annealed at different temperatures (the inset is the schematic of the device structure, indicating the device active area), (b) short circuit current densities (J_{sc}) of PSCs as a function of the annealing temperature, (c) PCE of perovskite solar cells as a function of the annealing temperature, and (d) open circuit voltage (V_{oc}) of PSCs as a function of the annealing temperature.

TABLE II. Summary of the device characteristic parameters (PCEs, J_{sc} , V_{oc} , and FF) with the best, average, and standard deviation values.

Temperature (°C)	J_{sc} (mA cm ⁻²)	V_{oc} (V)	FF	PCE (%)
100	21.81 (20.52 ± 0.80)	1.011 (0.937 ± 0.073)	0.630 (0.560 ± 0.056)	13.56 (10.96 ± 1.80)
120	22.16 (19.69 ± 1.40)	1.002 (0.958 ± 0.034)	0.640 (0.580 ± 0.035)	14.37 (11.08 ± 1.37)
130	24.10 (23.10 ± 1.40)	1.080 (1.054 ± 0.031)	0.690 (0.620 ± 0.037)	19.40 (17.79 ± 1.56)
140	20.36 (18.73 ± 1.41)	0.978 (0.922 ± 0.041)	0.561 (0.492 ± 0.050)	14.51 (9.28 ± 2.12)
150	17.34 (11.93 ± 4.70)	0.889 (0.798 ± 0.052)	0.482 (0.411 ± 0.046)	7.44 (4.44 ± 1.96)

IV. SUMMARY AND CONCLUDING REMARKS

We have shown that the percentage compositions of Ti and I mirror each other in the *m*-TiO₂ lattice. Hence, I substitutes at the Ti sites, as the annealing temperature increases. The Ti content decreases with increasing annealing temperature (from 100 to 130 °C), while the I content increases with increasing annealing temperature between 140 and 150 °C. The diffusion of I as well as Pb to the mesoporous layer has the potential to reduce oxygen vacancies for improved charge extraction between 100 and 130 °C annealing temperatures. Interdiffusion also results in a dramatic increase in the Ti and Sn contents in the perovskite film with increasing annealing temperature.

Significant strains are induced by the annealing of PSCs. The strains are associated with grain growth and the interdiffusion of constituent elements. However, the strains are generally insufficient to cause cracking or void formation during annealing at temperatures between 100 and 130 °C. In contrast, annealing at higher temperatures between 140 and 150 °C results in the formation of cracks and voids that degrade the performance of the PSCs.

The increased grain sizes obtained after annealing at temperatures between 100 and 130 °C are associated with increasing charge extraction, lower levels of charge recombination, and changes in the film crystallinity. These enable the improvement of the PCEs of the champion PSC devices to increase from 13.56% to 19.4%, as the annealing temperatures increase between 100 and 130 °C. However,

the defects (cracks and voids) formed at higher annealing temperatures between 140 and 150 °C act as carrier recombination sites, which drastically reduce the efficiencies of the PSCs from 19.4% to 7.44%.

SUPPLEMENTARY MATERIAL

See the [supplementary material](#) for detailed cross-sectional SEM images of the layered films, EDX spectra in mesoporous TiO₂ and perovskite layers, histograms of grain areas of perovskite films, and PCEs of the devices annealed at different temperatures.

ACKNOWLEDGMENTS

The authors are grateful to the Pan African Materials Institute of the World Bank African Centers of Excellence Program (Grant No. P126974) and the Worcester Polytechnic Institute for financial support.

DATA AVAILABILITY

The data that support the findings of this study are available from the corresponding author upon reasonable request.

REFERENCES

- 1 A. Kojima, K. Teshima, Y. Shirai, and T. Miyasaka, *J. Am. Chem. Soc.* **131**, 6050 (2009).
- 2 H. S. Kim, C. R. Lee, J. H. Im, K. B. Lee, T. Moehl, A. Marchioro, S. J. Moon, R. Humphry-Baker, J. H. Yum, J. E. Moser, M. Grätzel, and N. G. Park, *Sci. Rep.* **2**, 591 (2012).
- 3 W. S. Yang, J. H. Noh, N. J. Jeon, Y. C. Kim, S. Ryu, J. Seo, and S. Il Seok, *Science* **348**, 1234 (2015).
- 4 J. H. Heo, S. H. Im, J. H. Noh, T. N. Mandal, C.-S. Lim, J. A. Chang, Y. H. Lee, H.-j. Kim, A. Sarkar, M. K. Nazeeruddin, M. Grätzel, and S. Il Seok, *Nat. Photonics* **7**, 486 (2013).
- 5 K.-G. Lim, H.-B. Kim, J. Jeong, H. Kim, J. Y. Kim, and T.-W. Lee, *Adv. Mater.* **26**, 6461 (2014).
- 6 K.-G. Lim, S. Ahn, Y.-H. Kim, Y. Qi, and T.-W. Lee, *Energy Environ. Sci.* **9**, 932 (2016).
- 7 K. G. Lim, S. Ahn, H. Kim, M. R. Choi, D. H. Huh, and T. W. Lee, *Adv. Mater. Interfaces* **3**, 1500678 (2016).
- 8 M. A. Green, A. Ho-Baillie, and H. J. Snaith, *Nat. Photonics* **8**, 506 (2014).
- 9 M. Grätzel, *Nat. Mater.* **13**, 838 (2014).
- 10 N.-G. Park, *J. Phys. Chem. Lett.* **4**, 2423 (2013).
- 11 N. J. Jeon, J. H. Noh, Y. C. Kim, W. S. Yang, S. Ryu, and S. Il Seok, *Nat. Mater.* **13**, 897 (2014).
- 12 J. Qing, H.-T. Chandran, Y.-H. Cheng, S.-W. Tsang, M.-F. Lo, and C.-S. Lee, *Org. Electron.* **38**, 144 (2016).
- 13 W. Zhao, S. Li, H. Yao, S. Zhang, Y. Zhang, B. Yang, and J. Hou, *J. Am. Chem. Soc.* **139**, 7148 (2017).
- 14 M. Saliba, T. Matsui, J.-Y. Seo, K. Domanski, J.-P. Correa-Baena, M. K. Nazeeruddin, S. M. Zakeeruddin, W. Tress, A. Abate, A. Hagfeldt, and M. Grätzel, *Energy Environ. Sci.* **9**, 1989 (2016).
- 15 G. Li, V. Natu, T. Shi, M. W. Barsoum, and L. V. Titova, *ACS Appl. Energy Mater.* **3**, 1530 (2020).
- 16 N. J. Jeon, J. H. Noh, W. S. Yang, Y. C. Kim, S. Ryu, J. Seo, and S. Il Seok, *Nature* **517**, 476 (2015).
- 17 T. Jesper Jacobsson, J.-P. Correa-Baena, M. Pazoki, M. Saliba, K. Schenk, M. Grätzel, and A. Hagfeldt, *Energy Environ. Sci.* **9**, 1706 (2016).
- 18 K. T. Cho, S. Paek, G. Grancini, C. Roldán-Carmona, P. Gao, Y. Lee, and M. K. Nazeeruddin, *Energy Environ. Sci.* **10**, 621 (2017).
- 19 G. E. Eperon, S. D. Stranks, C. Menelaou, M. B. Johnston, L. M. Herz, and H. J. Snaith, *Energy Environ. Sci.* **7**, 982 (2014).
- 20 J.-Y. Jeng, Y.-F. Chiang, M.-H. Lee, S.-R. Peng, T.-F. Guo, P. Chen, and T.-C. Wen, *Adv. Mater.* **25**, 3727 (2013).
- 21 NREL. National Renewable Energy Laboratory Photovoltaic Research: Best Research-Cell Efficiency Chart (2020), <https://www.nrel.gov/pv/cell-efficiency.html>.
- 22 M. J. P. Alcocer, T. Leijtens, L. M. Herz, A. Petrozza, and H. J. Snaith, *Science* **342**, 341 (2013).
- 23 C. Wehrenfennig, G. E. Eperon, M. B. Johnston, H. J. Snaith, and L. M. Herz, *Adv. Mater.* **26**, 1584 (2014).
- 24 L. C. Chen, J. R. Wu, Z. L. Tseng, C. C. Chen, S. H. Chang, J. K. Huang, K. L. Lee, and H. M. Cheng, *Materials* **9**, 747 (2016).
- 25 D. Chen, X. Zou, H. Yang, N. Zhang, W. Jin, X. Bai, and Y. Yang, *Int. J. Photoenergy* **2017**, 7190801.
- 26 A. Dualeh, N. Tétreault, T. Moehl, P. Gao, M. K. Nazeeruddin, and M. Grätzel, *Adv. Funct. Mater.* **24**, 3250 (2014).
- 27 H. S. Kim, I. Mora-Sero, V. Gonzalez-Pedro, F. Fabregat-Santiago, E. J. Juarez-Perez, N. G. Park, and J. Bisquert, *Nat. Commun.* **4**, 2242 (2013).
- 28 W. Qiu, A. Ray, M. Jaysankar, T. Merckx, J. P. Bastos, D. Cheyns, R. Gehlhaar, J. Poortmans, and P. Heremans, *Adv. Funct. Mater.* **27**, 1700920 (2017).
- 29 D. Bi, W. Tress, M. I. Dar, P. Gao, J. Luo, C. Renevier, K. Schenk, A. Abate, F. Giordano, J. P. Correa Baena, J. D. Decoppet, S. M. Zakeeruddin, M. K. Nazeeruddin, M. Grätzel, and A. Hagfeldt, *Sci. Adv.* **2**, e1501170 (2016).
- 30 J.-P. Correa-Baena, M. Anaya, G. Lozano, W. Tress, K. Domanski, M. Saliba, T. Matsui, T. J. Jacobsson, M. E. Calvo, A. Abate, M. Grätzel, H. Miguez, and A. Hagfeldt, *Adv. Mater.* **28**, 5031 (2016).
- 31 J. Qing, H.-T. Chandran, H.-T. Xue, Z.-Q. Guan, T.-L. Liu, S.-W. Tsang, M.-F. Lo, and C.-S. Lee, *Org. Electron.* **27**, 12 (2015).
- 32 J. Burschka, N. Pellet, S.-J. Moon, R. Humphry-Baker, P. Gao, M. K. Nazeeruddin, and M. Grätzel, *Nature* **499**, 316 (2013).
- 33 M. Nagai, W. Gao, W. Huang, H. Yamamoto, and Y. Yoshida, *ECS J. Solid State Sci. Technol.* **5**, Q244 (2016).
- 34 Y.-M. Xie, C. Ma, X. Xu, M. Li, Y. Ma, J. Wang, H. T. Chandran, C.-S. Lee, and S.-W. Tsang, *Nano Res.* **12**, 1033 (2019).
- 35 J. Ye, H. Zheng, L. Zhu, X. Zhang, L. Jiang, W. Chen, G. Liu, X. Pan, and S. Dai, *Sol. Energy Mater. Sol. Cells* **160**, 60 (2017).
- 36 D. Barrit, P. Cheng, K. Darabi, M. C. Tang, D. M. Smilgies, S. Liu, T. D. Anthopoulos, K. Zhao, and A. Amassian, *Adv. Funct. Mater.* **30**, 1907442 (2020).
- 37 N. Kumari, S. R. Patel, and J. V. Gohel, *Optik* **176**, 262 (2019).
- 38 L. Huang, Z. Hu, J. Xu, K. Zhang, J. Zhang, and Y. Zhu, *Sol. Energy Mater. Sol. Cells* **141**, 377 (2015).
- 39 M.-F. Xu, H. Zhang, S. Zhang, H. L. Zhu, H.-M. Su, J. Liu, K. S. Wong, L.-S. Liao, and W. C. H. Choy, *J. Mater. Chem. A* **3**, 14424 (2015).
- 40 A. Klasen, P. Baumli, Q. Sheng, E. Johannes, S. A. Bretschneider, I. M. Hermes, V. W. Bergmann, C. Gort, A. Axt, S. A. L. Weber, H. Kim, H. Butt, W. Tremel, and R. Berger, *J. Phys. Chem. C* **123**(22), 13458–13466 (2019).
- 41 L. Xie, P. Vashishtha, T. M. Koh, P. C. Harikesh, N. F. Jamaludin, A. Bruno, T. J. N. Hooper, J. Li, Y. F. Ng, S. G. Mhaisalkar, and N. Mathews, *Adv. Mater.* **32**, 2003296 (2020).
- 42 F. Zhang, W. Shi, J. Luo, N. Pellet, C. Yi, X. Li, X. Zhao, T. J. S. Dennis, X. Li, S. Wang, Y. Xiao, S. M. Zakeeruddin, D. Bi, and M. Grätzel, *Adv. Mater.* **29**, 1606806 (2017).
- 43 C. Sun, Z. Wu, H. L. Yip, H. Zhang, X. F. Jiang, Q. Xue, Z. Hu, Z. Hu, Y. Shen, M. Wang, F. Huang, and Y. Cao, *Adv. Energy Mater.* **6**, 1670029 (2016).
- 44 S. Luo, P. You, G. Cai, H. Zhou, F. Yan, and W. A. Daoud, *Mater. Lett.* **169**, 236 (2016).
- 45 C. Li, Z. Zhu, B. Niu, F. Yang, X. Chen, Y. Ren, P. Zhong, S. Hayase, T. Cui, and R. Yang, *ACS Appl. Mater. Interfaces* **12**(31), 35105–35112 (2020).
- 46 J. E. Northrup, *Phys. Rev. B* **76**, 245202 (2007).
- 47 J. Xi, Z. Wu, B. Jiao, H. Dong, C. Ran, C. Piao, T. Lei, T. B. Song, W. Ke, T. Yokoyama, X. Hou, and M. G. Kanatzidis, *Adv. Mater.* **29**, 1606964 (2017).
- 48 H. Zhang, J. Shi, J. Dong, X. Xu, Y. Luo, D. Li, and Q. Meng, *J. Energy Chem.* **24**, 707 (2015).

- ⁴⁹Z. Xiao, C. Bi, Y. Shao, Q. Dong, Q. Wang, Y. Yuan, C. Wang, Y. Gao, and J. Huang, *Energy Environ. Sci.* **7**, 2619 (2014).
- ⁵⁰C. Bi, Y. Shao, Y. Yuan, Z. Xiao, C. Wang, Y. Gao, and J. Huang, *J. Mater. Chem. A* **2**, 18508 (2014).
- ⁵¹M.-C. Jung and Y. Qi, *Org. Electron.* **31**, 71 (2016).
- ⁵²M. C. Jung, S. R. Raga, L. K. Ono, and Y. Qi, *Sci. Rep.* **5**, 9863 (2015).
- ⁵³X. Ma, P. Tang, D. Liu, J. Zhang, L. Feng, and L. Wu, *ChemPhysChem* **18**, 2939 (2017).
- ⁵⁴C. Liu, D. Zhang, Z. Li, W. Han, G. Ren, Z. Li, L. Shen, W. Guo, and W. Zheng, *Sol. RRL* **4**, 1900489 (2020).
- ⁵⁵O. V. Oyelade, O. K. Oyewole, D. O. Oyewole, S. A. Adeniji, R. Ichwani, D. M. Sanni, and W. O. Soboyejo, *Sci. Rep.* **10**, 7183 (2020).
- ⁵⁶H. Mohammadian-Sarcheshmeh and M. Mazloum-Ardakani, *Heliyon* **4**, e00912 (2018).
- ⁵⁷V. Sivaram, E. J. W. Crossland, T. Leijtens, N. K. Noel, J. Alexander-Webber, P. Docampo, and H. J. Snaith, *J. Phys. Chem. C* **118**, 1821 (2014).
- ⁵⁸X. Lü, X. Mou, J. Wu, D. Zhang, L. Zhang, F. Huang, F. Xu, and S. Huang, *Adv. Funct. Mater.* **20**, 509 (2010).
- ⁵⁹M. Lai, A. Obliger, D. Lu, C. S. Kley, C. G. Bischak, Q. Kong, T. Lei, L. Dou, N. S. Ginsberg, D. T. Limmer, and P. Yang, *Proc. Natl. Acad. Sci. U. S. A.* **115**, 11929 (2018).
- ⁶⁰K. S. Shim, H. K. Yang, B. K. Moon, J. H. Jeong, S. S. Yi, and K. H. Kim, *Appl. Phys. A* **88**, 623 (2007).
- ⁶¹K. G. Cho, D. Kumar, D. G. Lee, S. L. Jones, P. H. Holloway, and R. K. Singh, *Appl. Phys. Lett.* **71**, 3335 (1997).
- ⁶²J. Szczyrbowski and A. Czaplá, *Thin Solid Films* **46**, 127 (1977).
- ⁶³Y. Fang, Q. Dong, Y. Shao, Y. Yuan, and J. Huang, *Nat. Photonics* **9**, 679 (2015).
- ⁶⁴K. J. Karki, M. Abdellah, W. Zhang, and T. Pullerits, *APL Photonics* **1**, 046103 (2016).
- ⁶⁵M. K. Ahmad, N. A. Marzuki, C. F. Soon, N. Nafarizal, R. Sanudin, A. B. Suriani, A. Mohamed, M. Shimomura, K. Murakami, M. H. Mamat, and M. F. Malek, *AIP Conf. Proc.* **1788**, 030044 (2017).
- ⁶⁶Y. Zhao and K. Zhu, *J. Phys. Chem. Lett.* **4**, 2880 (2013).
- ⁶⁷F. Ma, J. Li, W. Li, N. Lin, L. Wang, and J. Qiao, *Chem. Sci.* **8**, 800 (2016).
- ⁶⁸S. Kavadiya, J. Strzalka, D. M. Niedzwiedzki, and P. Biswas, *J. Mater. Chem. A* **7**, 12790 (2019).
- ⁶⁹C. C. Stoumpos, C. D. Malliakas, and M. G. Kanatzidis, *Inorg. Chem.* **52**, 9019 (2013).
- ⁷⁰A. Acciaoli, G. Lionello, and M. Baleani, *Materials* **11**, 751 (2018).
- ⁷¹W. H. Peters and W. F. Ranson, *Opt. Eng.* **21**, 427 (1982).